aerospace

MDPI

Article

The Contrail Mitigation Potential of Aircraft Formation Flight Derived from High-Resolution Simulations

Simon Unterstrasser

Deutsches Zentrum für Luft- und Raumfahrt, Institut für Physik der Atmosphäre, Oberpfaffenhofen, 82234 Wessling, Germany; simon.unterstrasser@dlr.de

Received: 3 November 2020; Accepted: 1 December 2020; Published: 5 December 2020

Abstract: Formation flight is one potential measure to increase the efficiency of aviation. Flying in the upwash region of an aircraft's wake vortex field is aerodynamically advantageous. It saves fuel and concomitantly reduces the carbon foot print. However, CO_2 emissions are only one contribution to the aviation climate impact among several others (contrails, emission of H_2O and NO_x). In this study, we employ an established large eddy simulation model with a fully coupled particle-based ice microphysics code and simulate the evolution of contrails that were produced behind formations of two aircraft. For a large set of atmospheric scenarios, these contrails are compared to contrails behind single aircraft. In general, contrails grow and spread by the uptake of atmospheric water vapour. When contrails are produced in close proximity (as in the formation scenario), they compete for the available water vapour and mutually inhibit their growth. The simulations demonstrate that the contrail ice mass and total extinction behind a two-aircraft formation are substantially smaller than for a corresponding case with two separate aircraft and contrails. Hence, this first study suggests that establishing formation flight may strongly reduce the contrail climate effect.

Keywords: climate impact; aviation; formation flight; mitigation potential; large-eddy simulation LES; particle-based ice microphysics; wake vortex

1. Introduction

Formation flight (FF) is a well-known strategy of migratory birds in order to improve their aerodynamic efficiency, save energy and increase their range [1–3]. Similarly, FF can increase the performance in the civil and military aviation sector. In addition to close FF (with separations of a few wing spans in flight direction) in the military sector, extended FF (with separations of 10 to 40 wing spans) is a viable option for the commercial sector. Follower aircraft (AC) encounter uplift from flying in the upwash region created outboard of a leading AC. Numerous numerical, wind tunnel and real flight studies, e.g., [4–12] demonstrate that the induced drag is reduced, the lift-to-drag ratio increases and fuel consumption is lower. One goal of these studies is to find the lateral and vertical offset of the AC positions with maximum benefit (the so-called sweet spot).

Fuel savings of around 10% can be expected during such formations (on average over all participating AC, not only for the follower AC; see exhaustive list of references above). In order to establish formations in the airspace, re-routing is required. Clearly, re-routing induced fuel penalties should be substantially smaller than the fuel savings during the actual formation. Xu et al. [13] find net fuel burn reductions of nearly 8% and 6% for different network sizes of cooperating airlines.

Fuel savings directly translate into lower CO_2 emissions and would reduce the climate impact of aviation. Besides the emission of carbon dioxide, the formation of contrails and the emission of nitrogen oxides cause a substantial aviation radiative forcing [14,15] which would be both affected

by the introduction of FF. The contrail radiative forcing (RF) is probably larger than the RF of the total accumulated CO_2 emissions from aviation [16,17] and the present study focuses on the contrail mitigation potential by FF.

Contrails grow and spread by the uptake of atmospheric water vapour and the initial emission of water vapour contributes a minor fraction to the ice mass of the aged contrail-cirrus [18] and also to its radiative effect. Saturation effects can be expected when contrails of two or more aircraft are produced in close proximity as they compete for the available atmospheric water vapour and mutually inhibit their growth. Hence, their overall effect is smaller than in a situation with similar atmospheric conditions where each contrail evolved undisturbed of the others [19]. Note the difference to the CO_2-effect, where the impact is solely determined by the initial emissions as they simply accumulate.

In a recent study, the early evolution of contrails produced by two AC in formation was analysed and compared to classical contrails behind a single aircraft. Classical single aircraft (SA) contrails grow mainly in vertical direction due to the wake vortex descent in the first few minutes, e.g., [20–22]. In FF scenarios the individual contrails merge quickly after their formation into a single contrail (from now on abbreviated as FF contrail). Unterstrasser and Stephan [23] found the wake vortex dynamics to be more complex and diverse as vortex pairs happen to also move upwards and sideways. After vortex break-up, FF contrails are thus not as deep, yet they are broader than SA contrails. Earlier studies already demonstrated that differences in the early contrail properties triggered by differences in wake vortex characteristics can have a long lasting mark. Unterstrasser and Görsch [24], e.g., simulated contrails produced by various aircraft types and initial differences in ice crystal number and contrail depth lead to quantitative differences between the contrail-cirrus properties that remain over the total simulation period of 6 h.

We employ the large-eddy simulation (LES) model EULAG-LCM, which is an established code for performing high-resolution simulations of contrails. In this study, we will juxtapose the evolution of contrails generated by a single aircraft, on the one hand, and by a two-aircraft formation, on the other hand. First, an exemplary simulation is presented, then the contrail-cirrus evolution is discussed for selected atmospheric scenarios. Finally, the study evaluates the extent of saturation in the formation flight scenarios (as introduced above) for a large set of prescribed atmospheric scenarios.

2. Methods

This section introduces the employed model with its numerical set-up and defines properties that will be used in the later analysis. The setup of the contrail-cirrus simulations, also known as dispersion phase simulations, presented here is in many aspects similar to the one in Unterstrasser et al. [25,26]. Hence, we give only a short description here. More details on the numerical setup are given in the two latter references.

2.1. Model

For the numerical simulations, the model EULAG-LCM has been used. EULAG [27,28] is a non-hydrostatic anelastic LES model, which employs the positive definite advection scheme MPDATA [29,30]. The ice microphysical module LCM, based on Lagrangian tracking of ice crystals [31], is fully coupled to EULAG. The model version EULAG-LCM has been used for the simulation of natural cirrus and contrails. Application examples are studies of a mid-latitude cirrus cloud system with a special focus on aggregation [32] and the contrail evolution during the vortex phase [24,33]. Moreover, contrail-cirrus simulations have been presented in Unterstrasser et al. [25] and its interaction with surrounding natural cirrus has been analysed in Unterstrasser et al. [26].

In LCM, ice crystals (ICs) are represented by Lagrangian simulation particles (SIPs), where every SIP represents a large number of real IC with identical properties. In order to reduce the complexity of the present simulations and simplify their interpretation, several LCM components are switched off (like heterogeneous nucleation, aggregation, and radiation). Although the switched-off processes can strongly alter the evolution of natural and contrail-cirrus, e.g., [32,34–37], we will give arguments in the

discussion section why we do not believe that the omission of those processes introduces systematic biases in the comparison of formation flight and single aircraft scenarios. The basic microphysical processes considered in the present set-up are deposition/sublimation and sedimentation. Moreover, natural cirrus can form by homogeneous nucleation. For the ice crystal habit, we assume hexagonal columns. A (synoptic scale) spatially homogeneous updraught motion is prescribed via an external forcing term in the temperature equation in order to accommodate for the adiabatic temperature reduction. The temperature reduction results in an increase of the background relative humidity and of the excess moisture. Details of the forcing implementation can be found in Unterstrasser and Gierens [36].

2.2. Numerical Set-Up

The simulation set-up for the present study is similar to that of previous EULAG-LCM contrail-cirrus simulations [24–26]. A two dimensional model, whose domain is perpendicular to the direction of flight and represents some portion of the UT/LS (upper tropospheric/lower stratospheric) region, is used. In the vertical (z-)direction, the domain dimension is 2.5 km. In the horizontal (x-)direction, the domain dimension is 40 km or 80 km (depending on the strength of the vertical wind shear; higher wind shear leads to broader contrails). Uniform grid boxes with sizes $dx = dz = 10$ m span a regular Cartesian mesh. The total simulated time is 8 h. The dynamical time step Δt_{dyn} is 2 s or 1.25 s depending on the vertical wind shear and the nucleation time step Δt_{nuc} is always 0.4 s (nucleation is turned on only in simulations with Δt_{dyn} is 2 s). Table 1 summarises the default values of fundamental numerical and atmospheric parameters.

Table 1. Summary of numerical and atmospheric parameters of the simulations. The meaning of the various symbols is explained in the text.

Default Parameter Settings					
Quantity	**Value**	**Quantity**	**Value**	**Quantity**	**Value**
Numerical parameters					
$\Delta x, \Delta z$	10 m	L_x	40.32 km	L_z	2.5 km
Δt_{dyn}	1.25 or 2.0 s	Δt_{nuc}	0.4 s	t_{sim}	8 h
Atmospheric parameters					
N_{BV}	$10^{-2}\,\mathrm{s}^{-1}$	$\hat{u}$	$0.12\,\mathrm{m\,s}^{-1}$	p_0	298 hPa
T^*	217 K	d_{ISSR}	≈1200 m	$d_{\mathrm{up}} = d_{\mathrm{down}}$	≈600 m

The vertical temperature profiles corresponds to a stably stratified atmosphere; we prescribe a Brunt-Väisälä frequency N_{BV} of $10^{-2}\,\mathrm{s}^{-1}$, a value typical of the upper troposphere. Background turbulent velocity fields are taken from a-priori simulations and have a root mean square (rms) value $\hat{u} = \left[\sum_i \left(u_i^2 + w_i^2\right)\right]^{0.5} \approx 0.12\,\mathrm{m\,s}^{-1}$. Even without any turbulence forcing mechanism, $\hat{u}$ does not drop below $0.1\,\mathrm{m\,s}^{-1}$ and the turbulence intensity is quasi-constant over the simulated period see Figure 3 in [25].

An ice-supersaturated (ISS) layer of $d_{\mathrm{ISSR}} \approx 1.2$ km thickness and an initial relative humidity (with respect to ice) of $RH_{\mathrm{i},0}{}^*$ is prescribed between $z = 1000$ m and 2000 m (see Figure 1 top). Above and below this layer, $RH_{\mathrm{i},0}$ drops to 20% inside 500 m thick transition zones. Below this transition zone, a 500 m thick layer with $RH_{\mathrm{i},0} = 20\%$ follows. The initial relative humidity $RH_{\mathrm{i},0}{}^*$ is either 110% or 120%. The superscript "*" refers to the constant RH_{i} value in the ISS layer.

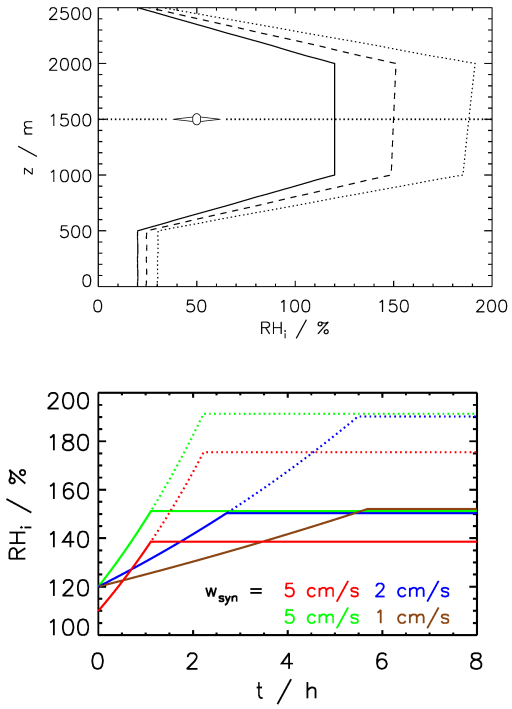

Figure 1. (**Top**): Vertical profile of the background relative humidity $RH_i{}^*(z)$ in the beginning (solid), after a 2 K cooling (dashed) or a 4 K cooling (dotted). The horizontal line at $z = 1500$ m indicates the flight altitude of the contrail-producing aircraft. This example shows the case with $RH_{i,0}{}^* = 120\%$. (**Bottom**): Temporal evolution of the background relative humidity $RH_i{}^*(t)$ at $z = 2000$ m for various updraught speeds $w_{syn} = 1\,\mathrm{cm\,s^{-1}}$ (brown), $2\,\mathrm{cm\,s^{-1}}$ (blue) and $5\,\mathrm{cm\,s^{-1}}$ (red and green). The initial $RH_{i,0}{}^*$ is either 110% or 120%. For $RH_{i,0}{}^* = 110\%$ only one scenario with $w_{syn} = 5\,\mathrm{cm\,s^{-1}}$ is displayed (red). The solid and dotted lines show scenarios with an adiabatic cooling of 2 K and 4 K, respectively.

The flight altitude of the contrail producing aircraft is at $z_{CA} = 1500$ m in the middle of the ISS layer resulting in $d_{up} = d_{down} \approx 600$ m thick fractions of the ISS layer above and below cruise altitude.

Three different synoptic scale updraught scenarios with w_{syn} either $= 1\,\mathrm{cm\,s^{-1}}, 2\,\mathrm{cm\,s^{-1}}$ or $5\,\mathrm{cm\,s^{-1}}$ are prescribed. By adjusting the updraught period, the prescribed final adiabatic cooling is either 2 K or 4 K and corresponds to an uplift of roughly 200 m or 400 m, respectively. Table 2 summarises the updraught velocities w_{syn} and durations t_{updr} of the various scenarios. The temporal evolution of the background relative humidity $RH_i{}^*(t)$ at $z = 2000$ m is shown in Figure 1 bottom. Three cases with $RH_{i,0}{}^* = 120\%$ and one case with $RH_{i,0}{}^* = 110\%$ are selected for display. In the 2 K scenarios, the peak RH_i is around 150% or 140% depending on $RH_{i,0}{}^*$. This is below or close to the threshold humidity where homogeneous nucleation starts. We deliberately switch off homogeneous nucleation in the 2 K scenarios (otherwise ICs might form in parts of the domain where turbulent fluctuations create RH_i values above the threshold) and hence contrails are the only cloud type in those simulations. In the 4 K scenarios, the ambient relative humidity rises well beyond the nucleation threshold and natural cirrus is allowed to form around the contrail. Homogeneous nucleation is initiated preferentially at the top of the supersaturated layer where the nucleation threshold humidity of $RH_{crit} \approx 155\%$ is surpassed first. The onset of cirrus formation t_{nuc} depends on w_{syn} (and to a lesser degree on $RH_{i,0}{}^*$) and is listed in Table 2. During the cirrus formation stage, up to 10×10^6 SIPs are generated to resolve the highly non-linear ice nucleation process. The stochastic nucleation implementation and an SIP merging technique as described in Unterstrasser and Sölch [38] are employed to increase numerical efficiency. In the very slow updraught scenario with $w_{syn} = 1\,\mathrm{cm\,s^{-1}}$ natural cirrus would form late in the simulated period and would not affect much the contrail evolution. Hence, 4 K cooling cases are only run for $w_{syn} = 2\,\mathrm{cm\,s^{-1}}$ or $5\,\mathrm{cm\,s^{-1}}$.

Table 2. Characteristics of the various updraught scenarios: updraught speed w_{syn}, updraught duration $t_{\mathrm{updr,2K}}$ and $t_{\mathrm{updr,4K}}$ for a 2 K or 4 K cooling, respectively and the approximate time of cirrus formation t_{nuc} for ${RH_{\mathrm{i,0}}}^* = 120\%$ and ${RH_{\mathrm{i,0}}}^* = 110\%$, respectively. The second block lists the final RH_{i} values ${RH_{\mathrm{i,f}}}^*$ as a function of ΔT and ${RH_{\mathrm{i,0}}}^*$.

Atmospheric Updraught Scenarios				
w_{syn} in cm s^{-1}	$t_{\mathrm{updr,2K}}$ in s	$t_{\mathrm{updr,4K}}$ in s	t_{nuc} / s ${RH_{\mathrm{i,0}}}^* = 120\%$	t_{nuc} / s ${RH_{\mathrm{i,0}}}^* = 110\%$
1	20,000	–	–	–
2	10,000	20,000	10,200	13,900
5	4000	8000	4000	5500
Final ${RH_{\mathrm{i}}}^*$				
	${RH_{\mathrm{i,0}}}^* = 110\%$		${RH_{\mathrm{i,0}}}^* = 120\%$	
$\Delta T = 2\,\mathrm{K}$	${RH_{\mathrm{i,f}}}^* = 139\%$		${RH_{\mathrm{i,f}}}^* = 151\%$	
$\Delta T = 4\,\mathrm{K}$	${RH_{\mathrm{i,f}}}^* = 175\%$		${RH_{\mathrm{i,f}}}^* = 191\%$	

Finally, we summarize aspects that differ from the original setup in Unterstrasser et al. [25]. In the original setup, a dry layer was also included above the upper transition zone. We found this layer to be irrelevant for the simulation results. Leaving it out, we could reduce the domain height from 3 km to 2.5 km. Originally, the flight altitude was close to the top of the ISS layer at $z_{\mathrm{CA}} = 2000\,\mathrm{m}$ with $d_{\mathrm{up}} = 200\,\mathrm{m}$ and $d_{\mathrm{down}} = 1000\,\mathrm{m}$. The present setup with $d_{\mathrm{up}} = d_{\mathrm{down}} \approx 600\,\mathrm{m}$ was tested in a sensitivity series called ISS_up. Moreover, it was necessary to slightly adapt the number of horizontal grid points nx from 4096 to 4032 due the changes in the supercomputing environment.

2.3. Contrail Initialisation

As in previous studies, the contrail initialisation is based on 3D data of contrail vortex phase simulations. The initialisation of a classical SA contrail is based on input data of Unterstrasser [33], whereas the corresponding simulations of an FF contrail-cirrus produced by a two-aircraft formation start with input data of Unterstrasser and Stephan [23].

The following presentation of the initial contrail properties is rather detailed as we will later see that the extent of saturation turns out to be sensitive to the contrail initialisation.

Generally, the contrail vortex phase features a vertical expansion of the contrail due to the downward moving wake vortex and potentially substantial ice crystal loss due to adiabatic heating. A summary of these processes and their sensitivity to atmospheric and aircraft parameters is given in Unterstrasser [22] and Paoli and Shariff [39].

Unterstrasser and Stephan [23] compare young contrails after vortex breakup produced behind a formation to those of the classical case. Qualitative differences were found: Behind a formation, the wake vortices of both aircraft interact. Often this leads to a strong lateral transport of one vortex pair and moderate sinking of the second pair. Hence, contrails behind a formation are broader, yet their vertical extent is smaller than in the classical case. Moreover, the ice crystal loss is not as pronounced as in the classical case.

All vortex phase simulations used as input in the present study use an ice crystal 'emission' index of $2.8 \times 10^{14}\,(\mathrm{kg\ fuel})^{-1}$ and the aircraft characteristics of an A350/B777 aircraft. Shortly after contrail formation, the SA contrail then consists of $\mathcal{N}_{00} = 3.4 \times 10^{12}$ ICs per meter of flight path, and in an FF contrail the number is just double as high ($\mathcal{N}_{00} = 6.8 \times 10^{12}\,\mathrm{m}^{-1}$). Due to crystal loss, the actual number decreases during the vortex phase. Columns 4 and 3 of Table 3 list the survival fraction f_{Ns} and the resulting IC number $\mathcal{N}_0$ with which the present simulations start. Clearly, $\mathcal{N}_0$ is smaller for smaller ${RH_{\mathrm{i,0}}}^*$. Moreover, the ice crystal number behind a formation is more than double as high as in the classical case, as fewer ICs are lost during the vortex phase. The factors $\mathcal{N}_{0,\mathrm{FF}}/\mathcal{N}_{0,\mathrm{SA}}$ are 4.5 and 2.6 for ${RH_{\mathrm{i,0}}}^* = 110\%$ and 120%, respectively.

Table 3. Initial contrail properties: f_{Ns} is the fraction of ice crystals that survive the vortex phase and is determined by $f_{\mathrm{Ns}} = \mathcal{N}_0/\mathcal{N}_{00}$. In the single aircraft case $\mathcal{N}_{00} = 3.4 \times 10^{12}\,\mathrm{m}^{-1}$ and in the formation flight scenario $\mathcal{N}_{00} = 6.8 \times 10^{12}\,\mathrm{m}^{-1}$.

Contrail Parameters						
scenario		# 1 W/m	# 2 H/m	# 3 $\mathcal{N}_0/(10^{12}\,\mathrm{m}^{-1})$	# 4 f_{Ns}	# 5 $\mathcal{I}_0/(\mathrm{kg/m})$
SA case REF @ ${RH_{\mathrm{i},0}}^* =$	110%	140	345	0.94	28%	0.05
	120%	250	420	2.22	66%	0.15
FF case @ ${RH_{\mathrm{i},0}}^* =$	110%	415	260	4.27	64%	0.17
	120%	430	260	5.91	89%	0.32
FF case ${RH_{\mathrm{i},0}}^* = 110\%$	DX45	400	260	2.74	41%	0.16
	DX55	590	250	3.68	55%	0.16
	DX60	610	270	3.33	49%	0.16

Figure 2 shows contrail IC number profiles in vertical (left) and transverse (right) direction. From the contrail profiles the contrail width W and vertical extent H are inferred and the values are also listed in Table 3 (columns 1 and 2). The solid curves shows the SA cases, where the contrail can extend up to 400 m below the flight altitude (in this plot $z = 0$ is identified with the flight altitude). For ${RH_{\mathrm{i},0}}^* = 110\%$, the contrail is considerably thinner since basically all ICs that were trapped in the downward sinking vortex system sublimate completely. In the FF scenarios, the contrail vertical extent ranges between 250 m and 300 m and is substantially smaller than for fully grown classical contrails. On the other hand, FF contrails are broader than SA contrails (400–600 m vs. 150–250 m). Moreover, large parts of the FF contrail can lie above cruise altitude. For this reason, the contrail is chosen to be located in the middle of the ISS layer in the contrail-cirrus simulations. If we had used the standard setup of Unterstrasser et al. [25] with $d_{\mathrm{up}} = 200\,\mathrm{m}$, the FF would penetrate into the transition zone, which is not desirable for a meaningful comparison between SA- and FF cases. Moreover, the various red lines illustrate the FF contrail sensitivity to parameters of the formation geometry, namely the lateral offset of the two AC in formation.

The number concentrations in young contrails are usually so high that the ambient supersaturation quickly relaxes to saturation as confirmed by contrail observations [40]. Hence, the ice water content scales linearly with the contrail volume and the ambient supersaturation. The listed initial ice mass values $\mathcal{I}_0$ reflect this fact. In particular, the FF cases have a higher initial ice mass as their volume is larger than that of classical contrails.

Next, we will shortly describe the technical procedure of how to incorporate the vortex phase simulation data in the model domain. The Eulerian 3D data (e.g., velocity (u, w), perturbations of water vapour concentration q_{v} and potential temperature θ) are averaged along flight direction and interpolated on the coarser grid and embedded into the enlarged 2D model domain. Lagrangian SIP data contain the information of the ICs and SIPs with similar positions (neglecting the coordinate y along flight direction) and IC sizes are merged. This reduces their overall number from several tens of millions in the 3D simulations to around 1.2×10^6 in the present approach. Unterstrasser and Sölch [38] showed that contrail-cirrus is sufficiently well represented by 1.2×10^6 SIPs for the type of analysis carried out in this study. Figure 3 exemplarily displays an initial 2D field, where the black box encompasses the area in which the 3D vortex phase data was inserted. In this example, relative humidity is shown. The RH_{i} values in the contrail are apparently lower than in the supersaturated environment, where the local RH_{i} values fluctuate around ${RH_{\mathrm{i},0}}^* = 120\%$.

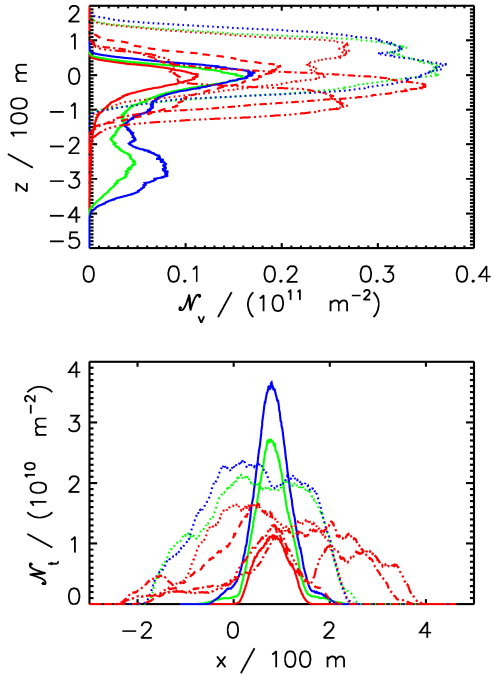

Figure 2. Contrail vertical and transverse ice crystal number profiles at initialisation for reference scenarios with a single aircraft (REF, solid) and formation flight scenarios with two aircraft (FF, all other line-styles). The initialisation data are taken from 3D vortex phase simulations, for REF from Unterstrasser [33] and for FF from Unterstrasser and Stephan [23]. Profiles are displayed for different initial ambient $RH_{\mathrm{i},0}{}^*$(110%, 120% or 140%: red, green, blue). For $RH_{\mathrm{i},0}{}^* = 110\%$, four different FF cases are shown (all red non-solid lines). The four cases are taken from a sensitivity study where the lateral separation DX of the two aircraft in formation was slightly varied ($DX = 45, 50, 55$ or 60 m). The flight altitude is at $z = 0$ and the single aircraft is centred around $x = 80$ m.

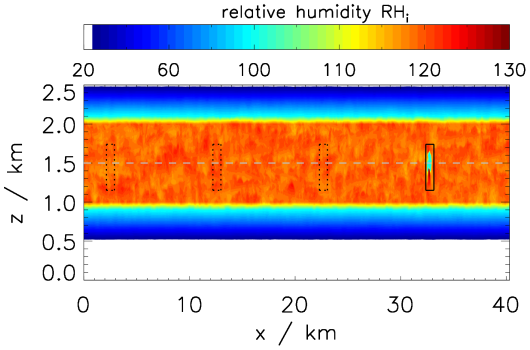

Figure 3. Initial RH_{i} field with the embedded vortex phase simulation result inside the 760 m × 600 m large black box. The dotted black boxes show alternative positions of the inital contrail placement. The grey horizontal line depicts the flight altitude. This example shows a case with $RH_{\mathrm{i},0}{}^* = 120\%$.

The SA simulations start with a 5 min old contrail as in previous studies. Behind a formation the wake vortices live longer and the present simulations start with a 7 min old FF contrail. Sensitivity tests using a 5 min old FF contrail showed similar results implying that the FF contrails basically reached their characteristic shape after 5 min and the IC loss has come to an end.

In the literature, the terms contrail and contrail-cirrus attempt to distinguish linear contrails from aged contrails that lost their line shape and whose appearance resembles those of natural cirrus. However, no clear definition can be made on what should be called contrail and what contrail-cirrus. In the following, the usage of the terms contrail and contrail-cirrus is not physically motivated; it should

simply ease the description of vortex phase simulations to simulate contrails, whereas dispersion phase simulations simulate contrail-cirrus (CC).

2.4. Set of Simulations

This subsection gives an overview over the complete set of simulations and clarifies which parameters and combinations of them are varied. For any given atmospheric scenario, simulations with SA contrail initialisations (REF) and FF contrail initialisation (FF) are performed.

As noted in the previous subsection, there are qualitative changes in contrail dimension and IC number between the REF and the FF initialisation. The later CC properties are affected by those initial differences as will be demonstrated in Section 3. To disentangle the effects of a variation of contrail dimension, on the one hand and of a variation of IC number, on the other hand, a third type of simulation referred to as NNN is introduced. The NNN simulations are based on the SA contrail initialisation and the contrail structure is thus identical to the REF case. The IC number concentrations are uniformly upscaled, such that the total IC number matches that of the corresponding FF scenarios. This upscale factor is 4.5 or 2.6 for $RH_{\mathrm{i},0}{}^{*} = 110\%$ or 120%, respectively.

The CC evolution and properties depend on many atmospheric parameters; several of them are chosen to determine what we call the atmospheric scenario. These are the initial relative humidity $RH_{\mathrm{i},0}{}^{*}$, the final adiabatic cooling ΔT, the updraught speed w_{syn} and the vertical wind shear $s = \partial u / \partial z$. Those parameters were selected because they are known to have a major impact on the CC life-cycle and/or they are expected to affect the relative differences between single-aircraft and formation flight CC. Other parameters that also affect the CC evolution like the initial temperature at flight altitude $T^{*} = 217\,\mathrm{K}$ are not varied. Those fixed parameters are listed in Table 1.

Table 4 gives a list of all parameter variations and combinations.

The first block of the section "Variation of the atmospheric scenario" lists all simulations with a final adiabatic cooling $\Delta T = 2\,\mathrm{K}$ where natural cirrus formation by homogeneous nucleation can be neglected and is suppressed in the model. For a moderate wind shear of $s = 0.002\,\mathrm{s}^{-1}$, the updraught speed w_{syn} takes the values 1, 2 and $5\,\mathrm{cm\,s}^{-1}$ and the initial relative humidity is either $RH_{\mathrm{i},0}{}^{*} = 110\%$ or 120%. Higher wind shear $s = 0.006\,\mathrm{s}^{-1}$ is used in one atmospheric scenario with $w_{\mathrm{syn}} = 5\,\mathrm{cm\,s}^{-1}$ and $RH_{\mathrm{i},0}{}^{*} = 120\%$.

The second block lists all simulations with a final adiabatic cooling $\Delta T = 4\,\mathrm{K}$ and natural cirrus formation around the CC. Wind shear is fixed at $s = 0.002\,\mathrm{s}^{-1}$, and all four combinations of $w_{\mathrm{syn}} = 2$ or $5\,\mathrm{cm\,s}^{-1}$ and $RH_{\mathrm{i},0}{}^{*} = 110\%$ or 120% are tested.

The second table section "Variation of the formation flight scenario" summarises the tests where the FF contrail initialisation is modified. Unterstrasser and Stephan [23] provides data of 3D simulations, where the two aircraft in the formation have a different vertical offset DZ and lateral offset DX. These changes affect the vortex trajectories and with it the early contrail structure. All non-solid red lines in Figure 2 depict the vertical and transverse profiles of simulations with varied DX (45, 50, 55, and 60 m). Those data are used as input and contrail-cirrus simulations have been performed for one selected atmospheric scenario with $RH_{\mathrm{i},0}{}^{*} = 110\%$, $w_{\mathrm{syn}} = 5\,\mathrm{cm\,s}^{-1}$, $\Delta T = 2\,\mathrm{K}$ and $s = 0.002\,\mathrm{s}^{-1}$.

Moreover, four different realisations of the same simulation are performed. To do so, the contrail location during the initialisation procedure is horizontally shifted relative to the background turbulence, i.e the location of the black box in Figure 3 changes (see the dotted boxes for the alternative contrail locations). Then, the contrail faces slightly changed turbulence structures which triggers initially small changes in the CC growth and spreading. Those small perturbation may or may not increase over time and the set of four realisations gives a notion of the spread of possible CC evolutions. In the present study, we do not focus on such aspects and only average values of the four realisations are analysed.

Overall, more than 130 CC simulations have been performed to account for the atmospheric variability and the turbulence induced uncertainty.

Table 4. Set of simulations: REF denotes reference simulations with a classical single aircraft contrail, FF the default formation flight simulation and NNN simulations of a classical single aircraft contrail with upscaled IC numbers matching those of corresponding FF simulations. In an FF sensitivity test, further formation flight scenarios are used as input and those simulations are referred to as FF_DX??, as the lateral offset DX of the two aircraft in formation was varied in preceding vortex phase simulations. Various atmospheric scenarios are listed: w01, w02 and w05 refers to an updraught speed $w_{\mathrm{syn}} = 1, 2$ and $5\,\mathrm{cm\,s^{-1}}$, s2 and s6 refers to wind shear $s = \partial u/\partial z = 0.002$ or $0.006\,\mathrm{s^{-1}}$. The initial relative humidity $RH_{\mathrm{i},0}{}^{*}$ is either 110% or 120%. Simulations without natural cirrus formation and final adiabatic cooling $\Delta T = 2\,\mathrm{K}$ use the code dt2K and simulations with natural cirrus formation around the CC use the code dT4K. The codes in parentheses or after the single braces starting with "F" refer to the number of the figure (and column) in which the simulation is depicted.

Variation of the Atmospheric Scenario			
simulation code	$RH_{\mathrm{i},0}{}^{*} = 110\%$	$RH_{\mathrm{i},0}{}^{*} = 120\%$	
w01_dT2K_s2	REF, FF, NNN (Figure 5c4)	REF, FF, NNN (Figure 5c3)	Figure 7c1, Figure 8
w02_dT2K_s2	REF, FF, NNN	REF, FF, NNN (Figure 5c2)	
w05_dT2K_s2	REF, FF, NNN (Figure 9)	REF, FF, NNN (Figure 4, Figure 5c1)	
w02_dT2K_s6	-	REF, FF, NNN (Figure 5c5)	
w02_dT4K_s2	REF, FF (Figure 6c3)	REF, FF (Figure 6c2)	Figure 7c2, Figure 8
w05_dT4K_s2	REF, FF	REF, FF (Figure 6c1)	
Variation of the Formation Flight Scenario			
Formation scenario	atmospheric scenario		
FF_DX45	w05_dT2K_s2 and $RH_{\mathrm{i},0}{}^{*} = 110\%$		Figure 9, Figure 10
FF or FF_DX50	w05_dT2K_s2 and $RH_{\mathrm{i},0}{}^{*} = 110\%$		
FF_DX55	w05_dT2K_s2 and $RH_{\mathrm{i},0}{}^{*} = 110\%$		
FF_DX60	w05_dT2K_s2 and $RH_{\mathrm{i},0}{}^{*} = 110\%$		

2.5. Analysed Quantities

In this final preparatory subsection, we define quantities that will be analysed in the subsequent results section.

The optical thickness $\tau(x)$ in a grid column is given by $\int_z \chi dz$, where $\chi(x, z)$ is the extinction coefficient of the all crystals in a grid box. The total extinction E of a CC is defined as

$$E = \int (1 - e^{-\tau})\, dx \approx \int \tau\, dx = \int \int \chi dz dx \tag{1}$$

The definition of CC width W_{OD} considers its visibility by a human observer. It counts all CC columns with $\tau > \tau_{\mathrm{vis}} = 0.02$. The mean optical thickness τ_m is the average of τ over all CC columns with $\tau \geq \tau_c = 0.005$. The total ice mass $\mathcal{I}$ is the integral of the ice mass concentration (IWC) over the contrail cross-section. Analogously, the total IC number $\mathcal{N}$ is derived from the IC number concentrations. Hence, $\mathcal{N}$ and $\mathcal{I}$ have units $\mathrm{m^{-1}}$ and $\mathrm{kg\ m^{-1}}$ (i.e., per meter of flight path). More information on the definitions can be found in Section 2.3 of Unterstrasser et al. [25].

The climate impact of a specific climate forcing is often measured in terms of a radiation perturbation at the top of the atmosphere (TOA), i.e., radiative forcing or effective radiative forcing [41,42]. Assessing the climate or contrail mitigation potential of formation flight, it would be favourable to evaluate the radiative forcing (RF) of the simulated contrails. However, this quantity cannot directly be derived from the present data as it requires further knowledge on the incident radiation fluxes, which are typically not characterised in LES setups.

Moreover, the contrail RF, which is given in units of W/m^2, typically quantifies the total radiative effect of all contrails inside a certain area and at a certain moment. It is not an ideal quantity for comparing the radiative effect of individual contrails as it does not take into account changes of the lifetime and its spatial extent. Integrating area-based quantities over the contrail length or horizontal extent and life cycle gives more meaningful quantities for the current approach, in analogy to the

energy forcing introduced by Schumann et al. [43,44]. The contrail-intrinsic properties that control its TOA radiative perturbation are the optical thickness τ and the effective radius r_{eff} [45], or equivalently τ and the ice water path IWP, which is the vertial integral of IWC. In analogy to the energy forcing, our proxy metrics for the comparison of the radiative impact of two contrail scenarios are then the time-integrated total extinction $\tilde{E}$ and total ice mass $\tilde{\mathcal{I}}$.

3. Results

3.1. Exemplary Simulation

First, we present snapshots of an exemplary SA simulation which show the CC cross-sections at initialisation and after 2, 4 and 8 h (Figure 4). The figure displays the extinction coefficient χ. The atmospheric conditions are $RH_{\text{i},0}{}^{*} = 120\%, w_{\text{syn}} = 5\,\text{cm}\,\text{s}^{-1}, \Delta T = 2\,\text{K}$ and $s = 0.002\,\text{s}^{-1}$. Here, the simulation time $t = 0\,\text{h}$ refers to a 5 min old contrail, cf. with Figure 1 of Unterstrasser [33]. The initial contrail is more than 450 m deep and nearly 300 m broad. The contrail is broadest in the lower part, where the Crow instability [46] leads to oscillations of the vortex tube along flight direction (over which is averaged here). Due to the prescribed wind shear, the CC gets tilted and spreads horizontally over time. The largest ICs start to settle and fall out from the tilted CC. A fall streak shapes up, with extinction values that are smaller than in the CC core region, i.e., the thin top layer with much higher χ values. The CC core region features high IC number densities and the fall streak is continuously fed by ICs that keep falling out of the CC core. Below the ISS layer, i.e., $z \lesssim 700\,\text{m}$, ICs shrink until they completely sublimate. Apparently, they disappear prior to reaching the lower domain boundary; we consider those ICs to be lost by sedimentation even though they are actually lost by sublimation. After 2 and 4 h, the width of the fully-grown CC attains values of 9 km and 17 km, respectively. The last snapshot after 8 h shows a decayed CC and the χ values are much smaller. A more detailed discussion of the CC evolution and its response to variations of the atmospheric background can be found in [18,25,26,36,37].

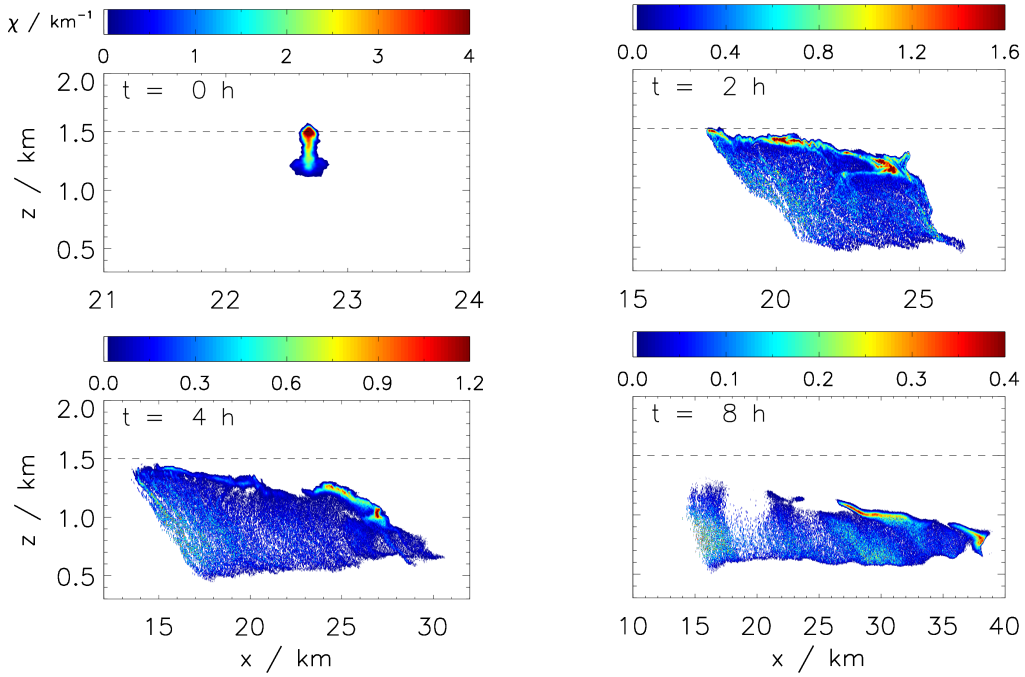

Figure 4. Contrail-cirrus cross-section coloured by the extinction coefficient χ at four different ages (see inserted time labels). Note that the ranges of the colour bars and the x-axes change over time as χ decreases in the spreading contrail-cirrus.

3.2. Contrail-Cirrus Evolution

Next, we showcase the variability of the CC evolution across various atmospheric scenarios and also highlight the differences between FF and REF scenarios.

For this, we choose five different quantities to be analysed in more detail. These are the total extinction E, the total ice mass $\mathcal{I}$, the total IC number $\mathcal{N}$, the mean optical thickness τ_m and the CC width W_{OD}. Figure 5 depicts only simulations with $\Delta T = 2\,\mathrm{K}$ and no natural cirrus formation. The black vertical bars in the upper row panels indicate the end of the prescribed updraught motion. The first three columns show simulations, where only the updraught speed, and with it the updraught period, is varied. The fourth column uses ${RH_{\mathrm{i},0}}^* = 110\%$ instead of ${RH_{\mathrm{i},0}}^* = 120\%$; otherwise the parameters are identical to column 3. The fifth column uses a stronger wind shear ($s = 0.006\,\mathrm{s}^{-1}$ instead of $0.002\,\mathrm{s}^{-1}$); all other simulation parameter are again identical to column 3. We first focus on ubiquitous features of the results, then on differences across the atmospheric scenarios, and finally on the differences between REF and FF scenarios.

Several features occur in all five simulations: The total extinction and the ice mass increase as long as the updraught prevails and atmospheric water vapour (WV) is supplied for IC growth. Clearly, after some hours the amount of ice mass is several orders of magnitude higher than the initial contribution from the emitted WV. Soon after the updraught comes to a halt, E and $\mathcal{I}$ start to decrease as sedimentation induced losses can no longer be compensated by WV uptake. The peak ice mass often amounts to more than 10 kg per meter of flight path. The IC number and the mean optical thickness decrease monotonically with time, in the first hour often at a much higher rate than later on. In the end, the mean optical thickness is below 0.1.

Next, we discuss the sensitivities to the atmospheric parameters.

If w_{syn} is reduced (columns 1 to 3), the peak and final values of E are higher, maximum CC width is larger, more ICs are lost in the first hour, for $t > 1\mathrm{h}$, however, the loss rates are smaller as fewer ICs are lost by sedimentation. If ${RH_{\mathrm{i},0}}^*$ is reduced (column 3 vs. 4), the lower IC number remains over the total simulation period. Similarly, all other quantities also attain smaller values for smaller ${RH_{\mathrm{i},0}}^*$. There are two reasons for this behaviour. First, the amount of supplied WV is smaller by one quarter, as can be derived from the ${RH_{\mathrm{i,f}}}^*$ values listed in Table 2 ($(1.39-1)/(1.51-1) \approx 0.75$). Second, shear-induced horizontal spreading is less effective for an initially shallower CC.

Lastly, vertical wind shear is increased (column 3 vs. 5). Note that the strong wind shear simulation is analysed only up to 5.5 h. Checking simulation snapshots of the type shown in Figure 4 reveals that a domain broader than 80 km would be necessary for a longer simulation time. Note that a simple example calculation ($\Delta W = s\,H\,\Delta t_{\mathrm{span}}$) shows that a $H = 1\,\mathrm{km}$ deep object broadens by around $\Delta W = 20\,\mathrm{km}$ during one hour $t_{\mathrm{span}} = 1\,\mathrm{h}$. Indeed, we observe that CC width increases much faster in the strong wind shear case. As a consequence, more WV can deposit on the ICs and total ice mass and extinction attain larger values. Moreover, stronger thinning leads to slightly smaller optical thickness values.

Next, we discuss qualitative differences between the REF and the FF cases. The major result is that the $\mathcal{I}$- and E curves of the FF cases lie substantially below the "REF * 2" curves implying strong saturation effects in formation flight scenarios. Often the FF curves are close to the REF curves, suggesting that initial differences in $\mathcal{N}_0$ and CC depth do not matter too much or compensate each other. The saturation effect comes, on first order, from the fact that in a formation two aircraft produce a single contrail that faces the same ambient conditions, in particular experiences the same WV supply, and evolves similarly to an SA CC.

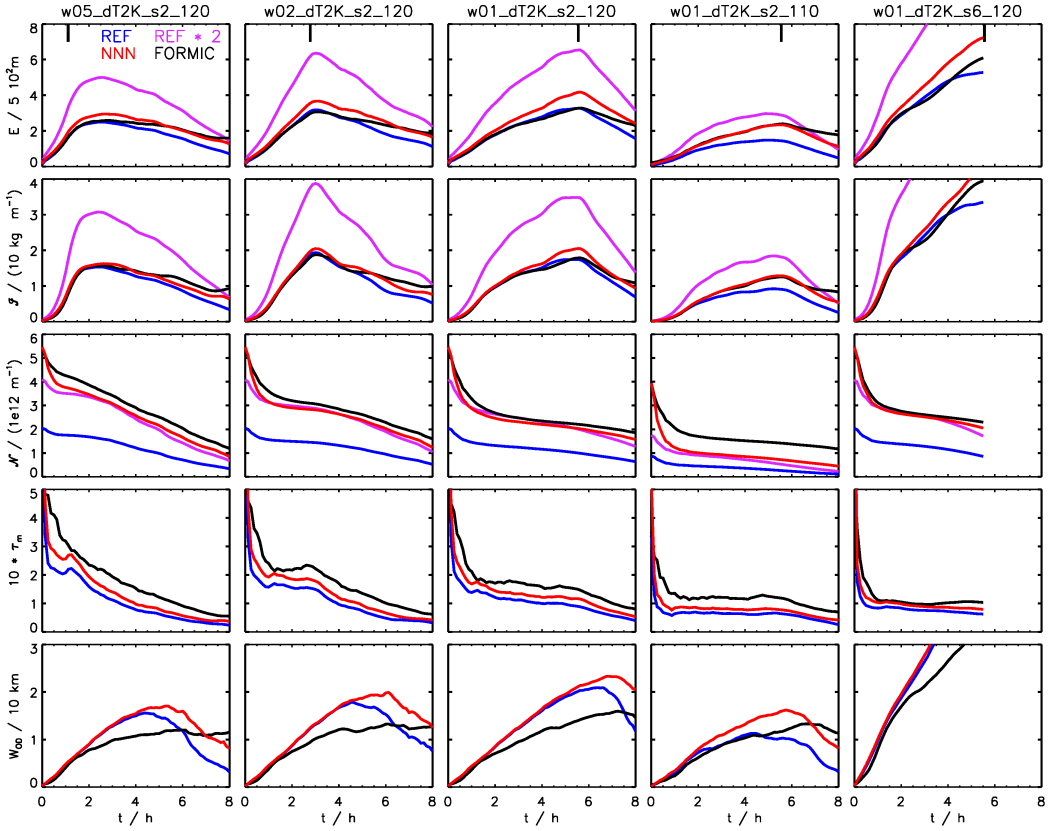

Figure 5. Temporal evolution of various contrail-cirrus properties are displayed for a selected set of simulation setups: total extinction E, total ice crystal mass $\mathcal{I}$ and number $\mathcal{N}$, optical thickness τ_m, and width W_{OD} (from top to bottom). The synoptic scenario is given on top of each panel. In this figure, $\Delta T = 2\,\mathrm{K}$ scenarios with no surrounding natural cirrus are displayed. The black bar indicates the time the synoptic scale updraught stops.

Moreover, we find a qualitatively different width evolution berween REF and FF. We first cover the four cases with ${RH_{\mathrm{i},0}}^* = 120\%$ (i.e., all but the fourth column). Within the first two hours the width increase is basically the same for REF and FF. Over the next few hours the REF CCs spread faster, a peak width value is attained after around 4 to 6 h, and width decreases from then on. The FF CCs spread at a lower rate compared to REF from $t = 2\,\mathrm{h}$ onwards, yet keeps increasing over (nearly) the total simulation time. Often, in the end FF CCs are broader than their REF counterparts.

In order to interpret the width evolution, two aspects have to be considered: First, how far are ICs transported by air motion and sedimentation? This determines the geometric cross-section (defined as the smallest polygon surrounding all CC ICs) and with it the geometric width. However, our width definition is based on visibility, hence the second question is: Are there enough ICs with sufficient ice mass in a specific column to be visible? The REF CCs are initially deeper, hence it seems reasonable that a stronger shear-induced spreading leads to the larger REF width values in the intermediate time period. The mean optical depth decreases over time, and towards the end an increasingly larger number of CC columns becomes sub-visual, hence W_{OD} decreases. In contrast, the geometric width of the FF CCs is smaller and there is less thinning. In combination with a higher IC number, the optical thickness hence remains above the visibility threshold τ_{vis} in most CC columns. This explanation is corroborated by the ${RH_{\mathrm{i},0}}^* = 110\%$ case in column 4. Due to IC loss, the initial SA contrail is shallower than for ${RH_{\mathrm{i},0}}^* = 120\%$ and the contrail depth value is closer to its FF counterpart. Then, we observe a very similar width evolution over the first five hours as the geometric width of FF and REF probably evolve similarly. After five hours, visible CC width keeps increasing only for FF, as the larger optical depth maintains visibility.

Finally, we discuss the NNN simulations, which help to disentangle effects of initial differences in contrail depth and IC number and will reinforce several arguments made above. By construction, NNN and FF simulations start with the same $\mathcal{N}_0$. Yet, the initial contrail dimensions are equal to REF. Due to the latter, we observe that contrail width of REF and NNN evolves basically identical. Only when the visibility aspect comes into play after several hours, the higher IC numbers and τ values result in a broader visible contrail in the NNN-cases. Moreover, the ice mass evolution of REF and NNN is similar, suggesting similar CC cross-sections and access to ambient supersaturation. In general, light scattering is increased if the same amount of ice mass is distributed over more ICs. For this reason, NNN simulations have higher E values than REF simulations. In most cases, the FF simulation lies in between of NNN and REF. Hence, the E values of the FF simulations are not as high as could be expected from the higher IC number. This implies that the weaker spreading of the FF CC partly offsets this increase in E. This finding helps to refine the above statement that initial differences in $\mathcal{N}_0$ and contrail depth do not matter too much. In fact, they partly cancel out each other and the net effect of both on the saturation extent is indeed of second order.

So far, scenarios with $\Delta T = 2\,\mathrm{K}$ have been discussed. Next, simulations with $\Delta T = 4\,\mathrm{K}$, where the formation of natural cirrus is allowed, are presented. To shorten the description only $E, \mathcal{I}$ and $\mathcal{N}$ are depicted in Figure 6. A detailed analysis of how CC and natural cirrus interact on a local scale and how CC evolution is affected by natural cirrus formation is given in Unterstrasser et al. [26] and the reader is referred to this paper for a deeper understanding. Inside the CC, relative humidity is too low to support nucleation of new ICs. ICs form only outside of the CC, once RH_i surpasses $RH_\mathrm{i,crit}$ of nucleation. Natural cirrus surrounds the CC and depletes WV in the vicinity of the CC. This confines the CC growth at its periphery. On the other hand, the sustained ascent continues to make more WV available inside the CC. Hence, in this region IC growth is stronger relative to the 2 K scenarios. These two counteracting effects lead apparently to the result that the E- and $\mathcal{I}$ evolutions do not differ much between a 4 K simulation and its respective 2 K counterpart (compare, e.g., first columns in Figures 5 and 6). Below the tilted CC, natural cirrus has been depleting the WV. This weakens the formation of the CC fall streak, as the contrail ice crystal do not grow as fast and sediment more slowly. For this reason, we find the number of ICs to decrease more slowly in the 4 K scenario as fewer ICs are lost by sedimentation.

Comparing the FF CC with REF CC, the findings are very similar to those of the 2 K scenarios. For ${RH_\mathrm{i,0}}^* = 120\%$ (columns 1 and 2) the FF CC are only slightly stronger in terms of E and $\mathcal{I}$ than the REF CC. Only in the case with ${RH_\mathrm{i,0}}^* = 110\%$, the E- and $\mathcal{I}$ values of the FF CC are substantially larger.

Figure 7 shows again E and $\mathcal{I}$, but now in a normalized version. For this, the FF simulation results are normalized by the "2 * REF" values, e.g, a value of 0.75 means that the "strength" of a contrail produced by an aircraft in a formation is only 75% of that by the same aircraft on a single mission. The added value of the normalized version is manifold. The compact form allows to include the complete set of investigated atmospheric scenarios, simplifies the comparison between FF and REF and nicely summarises conclusions made before. Furthermore, finally, it enables a quantitative comparison.

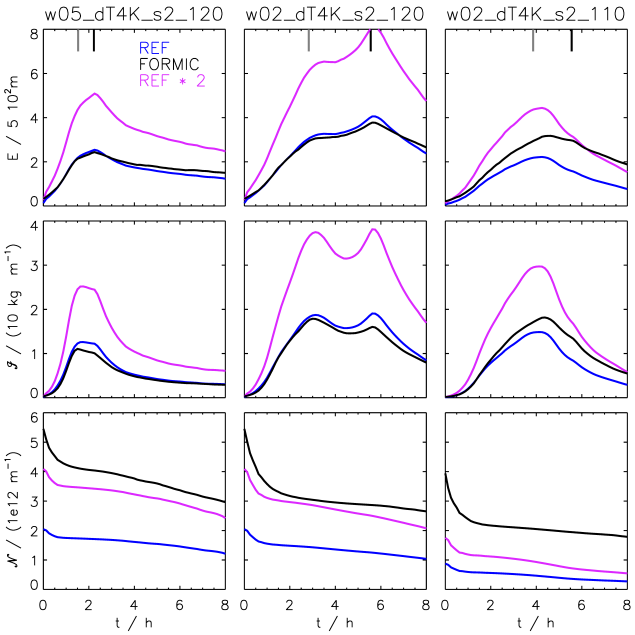

Figure 6. As in Figure 5, now for $\Delta T = 4\,\mathrm{K}$ scenarios with natural cirrus emerging around the contrail-cirrus. Unlike to Figure 5, no NNN simulations have been performed and neither optical thickness nor contrail width are shown. The grey bar additionally indicates the onset of natural cirrus formation.

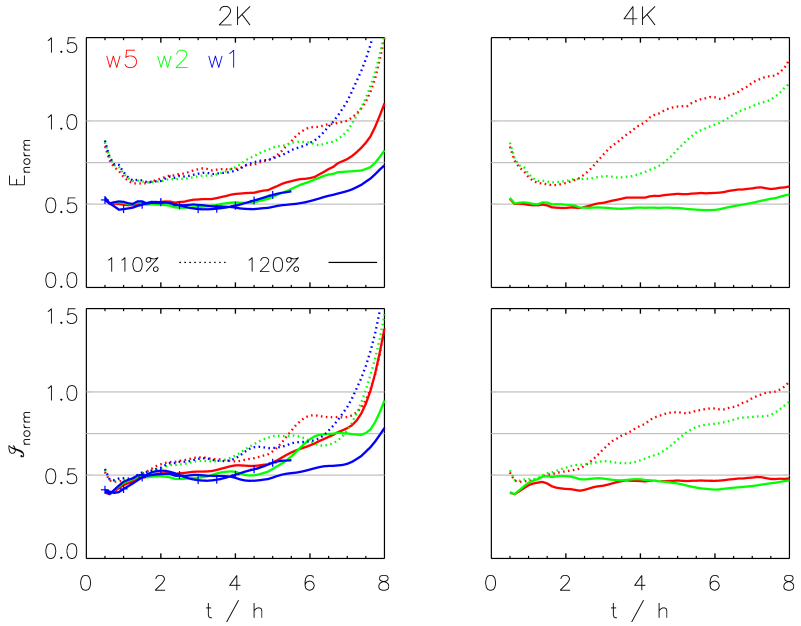

Figure 7. Temporal evolution of normalized total extinction and total ice mass. Unlike to Figure 5 where absolute values were shown, here the FF data are normalised by the 2 * REF data of the same atmospheric scenario. The left/right column shows scenarios with $\Delta T = 2\,\mathrm{K}$ and $\Delta T = 4\,\mathrm{K}$. The colour and line-style determine w_{syn} and $RH_{\mathrm{i},0}{}^{*}$ (see inserted legends in top left panel; "w5" e.g., stands for $w = 5\,\mathrm{cm\,s^{-1}}$). The curve with symbols shows the high wind shear case.

One apparent finding is that the normalized quantities have larger values (i.e., the saturation effect is less pronounced) for smaller RHi* as the dotted lines lie above the solid lines. In all $RH_{\mathrm{i},0}{}^{*} = 120\%$ cases (solid lines), the normalized values remain around 0.5 to 0.6 for many hours. In the 4 K cases (right column) it stays like this over the total simulations period. Only in the 2 K cases (left column),

the values increase towards the end. This is due to the fact that the FF CC dissolution is slower. However, one has to keep in mind, that the absolute values are already smaller in this stage. Hence, the relative importance of the normalized values on the time-integrated value is somewhat reduced. Now we switch to the $RH_{\mathrm{i},0}{}^{*} = 110\%$ cases (dotted lines). In the first hour the E_{norm} values drop from 0.85 to $0.65 - 0.70$ and then continuously increase over the total simulation period reaching values greater than unity in the end. The $\mathcal{I}_{\mathrm{norm}}$ values start from 0.5 and increase over time to roughly 1.

The CC evolution in absolute numbers depended dominantly s and w_{syn}. Interestingly, the normalized values, which spotlight the differences between REF and FF, are rather unaffected. This implies that REF and FF contrails respond similarly to changes in these atmospheric parameters.

In the first several minutes, the time series of E and $\mathcal{I}$ feature small wiggles. Moreover, they suffer from a systematic bias as the FF contrails are a few minutes older than the REF contrail at initialisation. This leads to irregular patterns and overestimates the normalized values E_{norm} and $\mathcal{I}_{\mathrm{norm}}$. Those irregularities are unimportant as the absolute values of E and $\mathcal{I}$ are still small. For this reason, E_{norm}- and $\mathcal{I}_{\mathrm{norm}}$ curves in Figure 7 are shown only for $t > 30\,\mathrm{min}$.

3.3. Time-Integrated Contrail Properties

So far, we assessed time series of contrail properties with the primary goal of explaining the physics behind the saturation effects. In the subsequent and final step of the present study, we analyse single-valued metrics to assess the saturation effect by formation flight. For this, we integrate E and $\mathcal{I}$ over time.

$$\tilde{X}_{\mathrm{scen}} = \int_{t=0}^{t_{\mathrm{int}}} X_{\mathrm{scen}}(t)\, dt,$$

where X stands for E or $\mathcal{I}$, and scen for REF, NNN or FF. In order to obtain normalized values $\hat{X}$, $\tilde{X}$ is divided by the time-integrated "2 * REF" value, i.e.,

$$\hat{X}_{\mathrm{scen}} = \frac{\tilde{X}_{\mathrm{scen}}}{2 \cdot \tilde{X}_{\mathrm{REF}}}.$$

The default integration period t_{int} is the total simulation period $t_{\mathrm{sim}} = 8\,\mathrm{h}$. Assuming that this time period represents a major fraction of the CC life-cycle, the obtained values serve as a measure of the CC radiative impact.

The prescribed ambient humidity evolution favours long contrail lifetimes, in particular for weak, but enduring updraughts. In the present simulations, CC dissolution is mainly triggered by sedimentation. ICs fall into the sub-saturated layer where they sublimate and the ISS layer above becomes dehydrated over time. In reality, ascending air masses may start to subside at some time and, as a result, CCs may start to vanish earlier than in our scenarios. Hence, CC lifetime is limited by sedimentation and/or subsidence as was specifically examined by Bier et al. [47]. To mimic scenarios with smaller contrail lifetimes, we do not perform additional simulations with scenarios that include a downdraught period and which would explicitly simulate the contrail dissolution. Instead, we choose a brute-force approach by analysing the existing simulations and simply shorten the integration period t_{int} in the above formulas. In addition to $t_{\mathrm{sim}} = 8\,\mathrm{h}$, values of 2 h, 4 h and 6 h are used.

Figure 8 shows absolute (top) and normalized (bottom) time-integrated total extinction (left) and total ice mass (right) for all scenarios. Scenarios with different ΔT (line-style), $RH_{\mathrm{i},0}{}^{*}$ (colour) and w_{syn} and s values (symbols) are depicted.

Let us first discuss the results of the upper row, which shows the time-integrated absolute total extinction and ice mass, respectively. Each curve connects four symbols showing the respective values for the different t_{int} values (2, 4, 6 and 8 h). Clearly, the values increase with increasing t_{int}. The initial relative humidity $RH_{\mathrm{i},0}{}^{*}$ and with it $RH_{\mathrm{i,f}}{}^{*}$ have the largest impact on $\tilde{E}$ and $\tilde{\mathcal{I}}$ (brown vs. red curves), whereas variations of ΔT (solid vs. dotted curves) and of w_{syn} (different symbols in one group of curves) tend to have a smaller impact. Qualitatively, the REF and FF scenarios seem to produce similar values. The lower row of Figure 8 presents normalized values. Again, FF values are divided by "2 *

REF". Hence, the depicted values provide a quantitative assessment of the saturation effects achieved by formation flight. The $\hat{E}$ values gather in two clusters: For ${RH_{\mathrm{i},0}}^* = 120\%$ the values lie in a narrow range around 0.5 and choices of $t_{\mathrm{int}}, \Delta T, w_{\mathrm{syn}}$ and s have little impact on the observed saturation. The by far largest impact on the saturation ratio has the initial relative humidity. For ${RH_{\mathrm{i},0}}^* = 110\%$ values lie mostly in the interval $[0.7, 0.8]$ and we can see a decrease in saturation for longer contrail lifetimes. Overall, we find that formation flight reduces the time-integrated total extinction by 20% to 50% (corresponding to $\hat{E} \in [0.5, 0.8]$). Compared to $\hat{E}$, the values of the metric $\hat{\mathcal{I}}$ are generally smaller, the parameter ${RH_{\mathrm{i},0}}^*$ is not as dominant and the sensitivity to t_{int} is larger. Overall, the time-integrated total ice mass is reduced by 30% to 60% (corresponding to $\hat{\mathcal{I}} \in [0.4, 0.7]$).

In Section 3.2, we mentioned two ways of how a variation of ${RH_{\mathrm{i},0}}^*$ affects the CC properties: the initial contrail properties and the amount of available ambient WV are changed. In the normalized quantities, the WV effect should, however, cancel out. Hence, the dominant impact of ${RH_{\mathrm{i},0}}^*$ is due to the fact that the initial contrail properties change with ${RH_{\mathrm{i},0}}^*$. This justifies a-posteriori the somewhat detailed presentation of the initial contrail properties given in Section 2.3 and Figure 2.

Two aspects of initial contrail properties differ between REF and FF, the geometric cross-section and the total number of ice crystals. The hybrid NNN simulations can help to answer the question which type of initial difference plays a bigger role for the long-lasting differences between FF- and SA CC. NNN simulations are initialized with the REF contrail, but with up-scaled IC number concentrations. In order to match the FF total IC number, the scaling factors are 4.5 and 2.6 for ${RH_{\mathrm{i},0}}^* = 110\%$ and 120%, respectively. The different scaling values explain why the $\hat{E}$ values of the NNN simulations are larger for ${RH_{\mathrm{i},0}}^* = 110\%$ than for ${RH_{\mathrm{i},0}}^* = 120\%$ (around 0.7 vs. 0.6). Moreover, we see that for ${RH_{\mathrm{i},0}}^* = 120\%$ the FF CC have smaller $\hat{E}$ values than the NNN CC. As mentioned in the subsequent section, this is probably due to the fact that the initial FF contrail is shallower. For ${RH_{\mathrm{i},0}}^* = 110\%$ the differences between the NNN and FF values are not as pronounced, as the initial depth of the REF/NNN and FF contrails is similar.

Overall, we conclude that in our scenarios formation flight leads to reductions in time-integrated total extinction and total ice mass by 20% to 50% and 30% to 60%, respectively. This implies a very large mitigation potential of formation flight.

3.4. Sensitivity to Formation Flight Geometry

The preceding Section 3.3 demonstrated that the derived saturation effects depend most strongly on the contrail properties after vortex breakup. There, the differences in early contrail properties were triggered by a variation of ${RH_{\mathrm{i},0}}^*$. As outlined in Section 2.3, geometric formation parameters like the horizontal offset DX of the two aircraft in formation also have an impact on the early FF contrail properties. So far, however, all presented FF simulations were based on one selected formation geometry with $DX = 50\,\mathrm{m}$. Hence, it is pending to check how strongly the derived saturation effects depend on the formation geometry. For this, we select one atmospheric scenario (as detailed in Section 2.4) and initialise the CC simulations with FF contrails with further DX values. Figure 9 shows results of those simulations ($DX = 45\,\mathrm{m}, 50\,\mathrm{m}, 55\,\mathrm{m}$ or $60\,\mathrm{m}$). The four panels on the left and in the middle show the temporal evolutions of $E, \mathcal{I}, \mathcal{N}$ and W_{OD} in absolute values, analogously to Figure 5. All four FF scenarios result in qualitatively similar contrail evolutions. Some differences are apparent in the width evolution from $t = 6\,\mathrm{h}$ onwards and initial differences in $\mathcal{N}$ remain over the complete simulation period. Yet, the radiatively important quantities E and $\mathcal{I}$ feature only a small spread across the FF scenarios. The panels on the right-hand side depict time series of E_{norm} and $\mathcal{I}_{\mathrm{norm}}$ in analogy to Figure 7 and confirm the modest to low sensitivity to the FF scenario. Finally, Figure 10 summarizes the above results in the two metrics, $\hat{E}$ and $\hat{\mathcal{I}}$. As in Figure 8, each curve connects four data points, which show values integrated over $t_{\mathrm{int}} = 2\,\mathrm{h}, 4\,\mathrm{h}, 6\,\mathrm{h}$ and $8\,\mathrm{h}$, respectively. $\hat{\mathcal{I}}$ values lie in the range between 0.5 and 0.65. Note that a variation of the atmospheric scenario for fixed ${RH_{\mathrm{i},0}}^* = 110\%$ produced $\hat{\mathcal{I}}$ values in the same range. Clearly, the sensitivity to the prescribed integration period t_{int} is

stronger than to the FF scenario. In particular for $t_{\mathrm{int}} = 2\,\mathrm{h}$, $\hat{I} \sim 0.52$ irrespective of DX. For higher t_{int}, $\hat{I}$ values exhibit some spread across the FF scenarios.

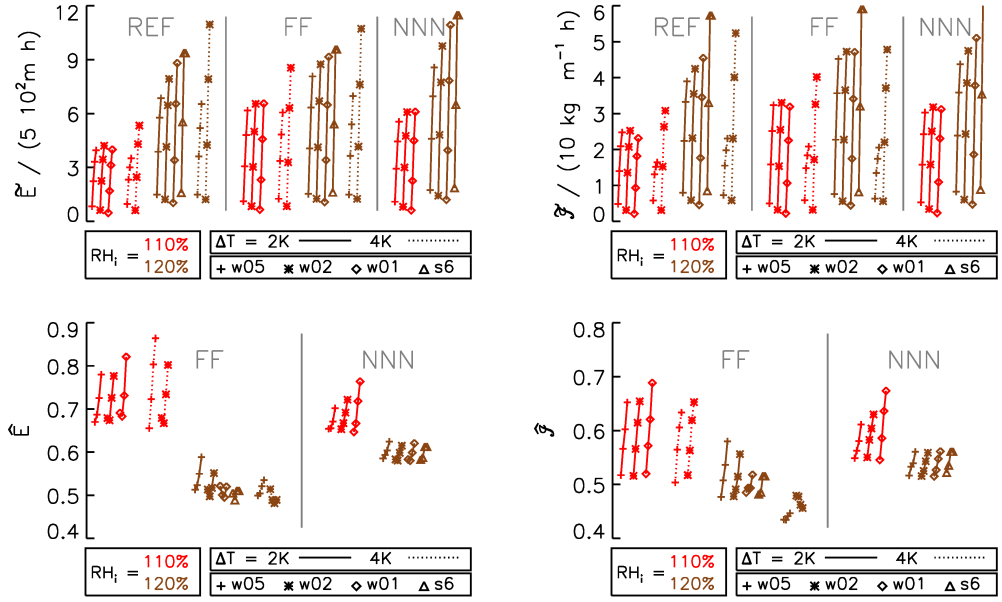

Figure 8. The extent of saturation in formation flight scenario is illustrated. Displayed are the time-integrated total extinction and total ice mass for lifetimes of 2, 4, 6 and 8 h along each curve. Top row: absolute values $\tilde{X}$, bottom row: normalised values $\hat{X}$; The symbols show absolute values for each of the REF, FF and NNN simulations (from left to right). The different symbols show various atmospheric scenarios (see symbols in legend) with $RH_{\mathrm{i},0}{}^{*} = 110\%$ (red) or 120% (brown). The solid/dotted lines show scenarios with $\Delta T = 2\,\mathrm{K}$ and 4 K, respectively. The set of scenarios is as in Figure 7. Each curve connects four identical symbols and is slightly slanted as the four symbols have a small horizontal offset. For each curve the integration time increases from left to right.

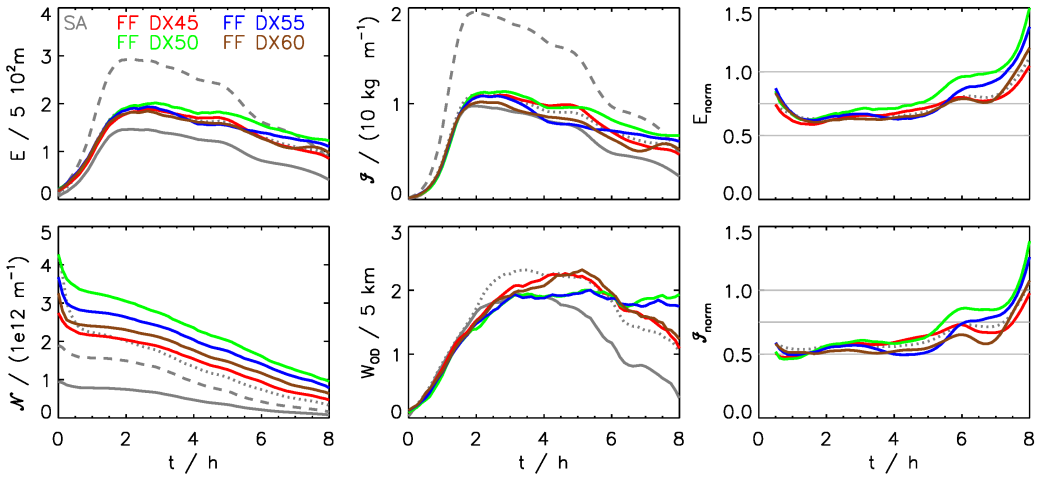

Figure 9. Temporal evolution of various contrail-cirrus properties are displayed for formation flight geometries with different lateral offset DX (ranging between 45 m and 60 m as indicated by the labels). The first two columns shows absolute values of total extinction, total ice crystal mass and number, and contrail width (analogous to Figure 5). The right-most column shows normalised values of total extinction and total ice crystal mass (analogous to Figure 7). The grey lines show the reference simulation REF (solid), 2 * REF (dashed) and NNN (dotted). The synoptic scenario is given by w05_dT2K_s2 and $RH_{\mathrm{i},0}{}^{*} = 110\%$ (see Table 4).

The extinction-based metric $\hat{E}$ reveals some dependence on the FF scenario. In particular, the default $DX = 50$ m simulation produces larger $\hat{E}$ values than the other DX simulations. The present finding may be a hint that the saturation effects can be larger (i.e., smaller $\hat{E}$) than what Figure 8 alone suggests as those simulations were solely based on $DX = 50$ m simulations.

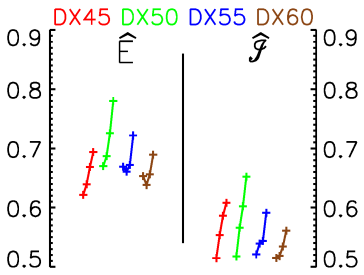

Figure 10. Time-integrated normalised total extinction $\hat{E}$ and total ice mass $\hat{\mathcal{I}}$ for formation flight geometries with different lateral offset DX (ranging between 45 m and 60 m, see colour legend on top). Similar to Figure 8, each curve connects four symbols that depict the values for lifetimes $t_{\mathrm{int}} = 2\,\mathrm{h}, 4\,\mathrm{h}, 6\,\mathrm{h}$ and 8 h.

4. Discussion

In this section we discuss implications and generalisations of our results and also assumptions and limits of the present study.

The saturation effect due to formation flight was evaluated for a multitude of atmospheric scenarios determined by w_{syn}, $RH_{\mathrm{i},0}{}^{*}$, s and ΔT. Those parameters were selected because they are known to have a strong impact on the CC life-cycle and/or they are expected to affect the relative differences between SA and FF CC. For example, the initial contrail depth H shows a characteristic difference between SA and FF scenario. Hence, SA and FF CC may respond differently to a change in vertical wind shear s as CC spreading depends on H and s. In general, we found that the extent of saturation is fairly insensitive to our variations of the atmospheric scenario or the formation geometry.

Astonishingly, the initial $RH_{\mathrm{i},0}{}^{*}$ was found to be the dominant parameter which deserves a closer investigation. A decrease in $RH_{\mathrm{i},0}{}^{*}$ leads to shallower contrails with fewer ice crystals, as most ice crystals in the primary wake sublimate during the early vortex descent. In particular, lowering $RH_{\mathrm{i},0}{}^{*}$ from 120% from 110%, as done here, leads to a strong reduction in the initial SA contrail depth see Figure 2 here or Figure 1 in [33]. Contrarily, the FF contrail depth does not change much with $RH_{\mathrm{i},0}{}^{*}$. Thus, the relative differences between the initial SA and FF contrails change substantially by a $RH_{\mathrm{i},0}{}^{*}$ change. Other parameters that have not been varied and potentially trigger relative differences between SA and FF cases may have a non-negligible impact on the observed saturation. These are parameters that affect the early contrail evolution and depth such as the aircraft type or the thermal stratification [24].

Our simulation setup, e.g., neglected several processes such as natural cirrus formation by heterogeneous nucleation, contrail radiative heating and aggregation. Even though this may affect the contrail-cirrus evolution, we do not expect that their neglect introduces biases in the comparison of SA and FF scenarios. Similarly, we do not expect that using a 2D-model domain instead of a 3D-model model [37,48] introduces systematic biases.

Moreover, we studied only formations of two identical aircraft and assumed equal emission characteristics for both. In particular, the fuel flow of the follower AC is not reduced, which neglects the reduction of WV emission and the number of generated ICs. Given that a much larger change of ice crystal number between the REF and NNN cases had only modest impact on the amount of saturation, a slight adaptation of fuel flow would result in only marginal changes.

In regions of dense air traffic a "natural" saturation effect occurs when several contrails overlap and form a contrail cluster. In such a case, it is not appropriate to choose an isolated contrail simulation as reference state and the saturation gain due to formation flight might be smaller than the ones we derived. On the other hand, we expect stronger saturation effects in formations with more than two aircraft.

We compare formation and single aircraft contrails at identical atmospheric scenarios. If formations generally fly, e.g., at a lower/higher altitude than the aircraft would do in solo missions, the systematic shift to higher/lower temperatures would affect the contrail properties. Possible biases by such re-routing induced changes of the atmospheric background state are not accounted for here.

The present work is to our knowledge the first study that estimates contrail saturation effect due to formation flight and as such provides a first estimate. It is out of scope to scan the full parameter space of contrail evolution. The implied accuracy of our saturation estimates is acceptable, having in mind, that transferring these numbers into global scale contrail models is done in a simplistic way and thus associated with further uncertainties. The LES-derived saturation values are fed into the non-linear climate response model AirClim [49]. Using realistic aircraft flight trajectories of single mission and formation flight emission scenarios [50] within AirClim provides a first global assessment of the formation flight mitigation potential [50,51].

5. Summary

This study presents high-resolution simulations of contrail-cirrus that originate from a single aircraft (SA) or a two-aircraft formation (FF). The simulations start with 5 to 7 min old contrails at a time when aircraft wake vortices decayed and the initial contrail data are provided by recent simulation study of early formation flight contrails [23]. The simulated time of 8 h covers large parts of the contrail-cirrus life-cycle.

The analysis focuses on determining the saturation effect that occurs when contrails of multiple aircraft are created in close proximity. Two single-valued metrics are defined in order to compare the contrail-cirrus evolution of SA cases, on the one hand, and FF cases, on the other hand, for a multitude of atmospheric scenarios.

The lifetime-integrated total extinction $\tilde{E}$ and total ice mass $\tilde{\mathcal{I}}$ behind a two-aircraft formation are found to be substantially smaller than for a corresponding case with two separate aircraft and contrails. In our scenarios, formation flight leads to reductions in $\tilde{E}$ and $\tilde{\mathcal{I}}$ by 20% to 50% and 30% to 60%, respectively.

The atmospheric scenarios include variations of the vertical wind shear, initial background relative humidity, the synoptic updraught speed and time period. Even though, variations of those parameters qualitatively change the contrail-cirrus evolution, the relative differences between SA and FF cases are fairly unaffected and the quantified magnitude of reduction seems to be valid for a wide range of situations. Interestingly, the dominant parameter is the initial relative humidity which affects more the early contrail properties than the later transition into contrail-cirrus. A variation of it provokes large relative differences in the early ice crystal number and contrail depth between the SA and FF cases.

Overall, the potential reductions by formation flight are quite substantial. This renders formation flight a promising measure to mitigate the contrail climate impact.

In companion papers of the FORMIC project (FORMation flight: Impact on Climate), the saturation values are fed into the non-linear climate response model AirClim [49]. AirClim also accounts for non-contrail aviation climate effects and was adopted to account for saturation effects occurring during formation flight [51]. Using realistic aircraft flight trajectories of single mission and formation flight emission scenarios [50] within AirClim provides a first global assessment of the formation flight mitigation potential [50,51].

Funding: This research was funded by the German Ministry of Economic Affairs and Energy (BMWi) under the National Aeronautical Research Programme (LuFo) V-2 under the grant agreement no. 20E1508C.

Acknowledgments: We thank S. Kaufmann for the comments on the manuscript draft. Computational resources were made available by the German Climate Computing Center (DKRZ) through support from the German Federal Ministry of Education and Research (BMBF).

Conflicts of Interest: The funders had no role in the design of the study; in the collection, analyses, or interpretation of data; in the writing of the manuscript, or in the decision to publish the results.

Abbreviations

The following abbreviations are used in this manuscript:

AC	aircraft
CC	contrail-cirrus
EULAG	name of the LES model
FF	formation flight
IC	ice crystal
ISS	ice-supersaturated
LCM	name of the ice microphysical model
LES	large-eddy simulation
NNN	type of REF simulation with upscaled IC number
RH_i	relative humidity with respect to ice
$RH_{\mathrm{i},0}{}^*$	initial background RH_i in the ISS layer
$RH_{\mathrm{i,f}}{}^{**}$	hypothetic background RH_i in the ISS layer after the synoptic cooling
REF	reference
RF	radiative forcing
SA	single aircraft
SIP	simulation particle
WV	water vapour

References

1. Lissaman, P.; Shollenberger, C. Formation flight of birds. *Science* **1970**, *168*, 1003–1005. [CrossRef] [PubMed]
2. Hummel, D. Aerodynamic aspects of formation flight in birds. *J. Theor. Biol.* **1983**, *104*, 321–347. [CrossRef]
3. Weimerskirch, H.; Martin, J.; Clerquin, Y.; Alexandre, P.; Jiraskova, S. Energy saving in flight formation. *Nature* **2001**, *413*, 697–698. [CrossRef] [PubMed]
4. Beukenberg, M.; Hummel, D. Aerodynamics, Performance and Control of Airplanes in Formation Flight. In Proceedings of the 17th Congress of the ICAS, Stockholm, Sweden, 9–14 September 1990; Volume 2, pp. 21777–21794.
5. Blake, W.; Multhopp, D. Design, performance and modeling considerations for close formation flight. In Proceedings of the Guidance, Navigation, and Control and Co-located Conferences, Boston, MA, USA, 10–12 August 1998; AIAA: Reston, VA, USA, 1998; p. 4343. [CrossRef]
6. Wagner, E.; Jacques, D.; Blake, W.; Pachter, M. Flight Test Results of Close Formation Flight for Fuel Savings. In Proceedings of the Guidance, Navigation, and Control and Co-located Conferences, Monterey, CA, USA, 5 August 2002; AIAA: Reston, VA, USA, 2002; p. 4490. [CrossRef]
7. Iglesias, S.; Mason, W. Optimum spanloads in formation flight. In Proceedings of the Aerospace Sciences Meetings, Reno, NV, USA, 14–17 January 2002; AIAA: Reston, VA, USA, 2002; p. 258. [CrossRef]
8. Frazier, J.W.; Gopalarathnam, A. Optimum Downwash Behind Wings in Formation Flight. *J. Aircraft* **2003**, *40*, 799–803. [CrossRef]
9. Bangash, Z.; Sanchez, R.; Ahmed, A.; Khan, M. Aerodynamics of formation flight. *J. Aircraft* **2006**, *43*, 907–912. [CrossRef]
10. Nangia, R.; Palmer, M. Formation Flying of Commercial Aircraft, Variations in Relative Size/Spacing—Induced Effects & Control Induced Effects & Control. In Proceedings of the Fluid Dynamics and Co-located Conferences, Miami, FL, USA, 25–28 June 2007; AIAA: Reston, VA, USA, 2007; p. 4163. [CrossRef]
11. Kless, J.E.; Aftosmis, M.J.; Ning, S.A.; Nemec, M. Inviscid Analysis of Extended-Formation Flight. *AIAA J.* **2013**, *51*, 1703–1715. [CrossRef]

12. Okolo, W.; Dogan, A.; Blake, W.B. A Modified Analysis of Alternate Lateral Trimming Methods for Flying Wing Aircraft at Sweet Spot in Formation Flight. In Proceedings of the AIAA SciTech Forum, National Harbor, MD, USA, 13–17 January 2014; AIAA: Reston, VA, USA, 2014; p. 0543. [CrossRef]
13. Xu, J.; Ning, S.; Bower, G.; Kroo, I. Aircraft Route Optimization for Formation Flight. *J. Aircraft* **2014**, *51*, 490–501. [CrossRef]
14. Sausen, R.; Isaksen, I.; Grewe, V.; Hauglustaine, D.; Lee, D.; Myhre, G.; Köhler, M.; Pitari, G.; Schumann, U.; Stordal, F.; et al. Aviation radiative forcing in 2000: An update on IPCC (1999). *Meteorol. Z.* **2005**, *14*, 555–561. [CrossRef]
15. Lee, D.; Pitari, G.; Grewe, V.; Gierens, K.; Penner, J.; Petzold, A.; Prather, M.; Schumann, U.; Bais, A.; Berntsen, T.; et al. Transport impacts on atmosphere and climate: Aviation. *Atmos. Environ.* **2010**, *44*, 4678–4734. [CrossRef]
16. Burkhardt, U.; Kärcher, B. Global radiative forcing from contrail cirrus. *Nat. Clim. Chang.* **2011**, *1*, 54–58. [CrossRef]
17. Bock, L.; Burkhardt, U. Reassessing properties and radiative forcing of contrail cirrus using a climate model. *J. Geophys. Res.* **2016**, *121*, 9717–9736. [CrossRef]
18. Unterstrasser, S.; Gierens, K. Numerical simulations of contrail-to-cirrus transition—Part 1: An extensive parametric study. *Atmos. Chem. Phys.* **2010**, *10*, 2017–2036. [CrossRef]
19. Unterstrasser, S.; Sölch, I. Numerical Modeling of contrail cluster formation. In Proceedings of the 3rd International Conference on Transport, Atmosphere and Climate, Prien, Deutschland, 25–28 June 2012; pp. 114–119.
20. Sussmann, R.; Gierens, K. Lidar and numerical studies on the different evolution of vortex pair and secondary wake in young contrails. *J. Geophys. Res.* **1999**, *104*, 2131–2142. [CrossRef]
21. Lewellen, D.; Lewellen, W. The effects of aircraft wake dynamics on contrail development. *J. Atmos. Sci.* **2001**, *58*, 390–406. [CrossRef]
22. Unterstrasser, S. Properties of young contrails—A parametrisation based on large-eddy simulations. *Atmos. Chem. Phys.* **2016**, *16*, 2059–2082. [CrossRef]
23. Unterstrasser, S.; Stephan, A. Far field wake vortex evolution of two aircraft formation flight and implications on young contrails. *Aeronaut. J.* **2020**, *124*, 667–702. [CrossRef]
24. Unterstrasser, S.; Görsch, N. Aircraft-type dependency of contrail evolution. *J. Geophys. Res.* **2014**, *119*, 14,015–14,027, 2014JD022642, [CrossRef]
25. Unterstrasser, S.; Gierens, K.; Sölch, I.; Lainer, M. Numerical simulations of homogeneously nucleated natural cirrus and contrail-cirrus. Part 1: How different are they? *Meteorol. Z.* **2017**, *26*, 621–642. [CrossRef]
26. Unterstrasser, S.; Gierens, K.; Sölch, I.; Wirth, M. Numerical simulations of homogeneously nucleated natural cirrus and contrail-cirrus. Part 2: Interaction on local scale. *Meteorol. Z.* **2017**, *26*, 643–661. [CrossRef]
27. Smolarkiewicz, P.; Margolin, L. On Forward-in-Time Differencing for Fluids: an Eulerian/Semi-Lagrangian Non-Hydrostatic Model for Stratified Flows. In *Numerical Methods in Atmospheric and Oceanic Modelling: The André J. Robert Memorial Volume*; Lin, C., Laprise, R., Ritchie, H., Eds.; Canadian Meteorological and Oceanographical Society: Ottawa, ON, Canada, 1997; Volume 35, pp. 127–152.
28. Smolarkiewicz, P.; Kühnlein, C.; Wedi, N. A consistent framework for discrete integrations of soundproof and compressible PDEs of atmospheric dynamics. *J. Comput. Phys.* **2014**, *263*, 185–205. [CrossRef]
29. Smolarkiewicz, P.; Margolin, L. MPDATA: A Finite-Difference Solver for Geophysical Flows. *J. Comput. Phys.* **1998**, *140*, 459–480. [CrossRef]
30. Smolarkiewicz, P.K. Multidimensional positive definite advection transport algorithm: an overview. *Int. J. Numer. Methods Fluids* **2006**, *50*, 1123–1144. [CrossRef]
31. Sölch, I.; Kärcher, B. A large-eddy model for cirrus clouds with explicit aerosol and ice microphysics and Lagrangian ice particle tracking. *Q. J. R. Meteorol. Soc.* **2010**, *136*, 2074–2093. [CrossRef]
32. Sölch, I.; Kärcher, B. Process-oriented large-eddy simulations of a midlatitude cirrus cloud system based on observations. *Q. J. R. Meteorol. Soc.* **2011**, *137*, 374–393. [CrossRef]
33. Unterstrasser, S. Large eddy simulation study of contrail microphysics and geometry during the vortex phase and consequences on contrail-to-cirrus transition. *J. Geophys. Res.* **2014**, *119*, 7537–7555. [CrossRef]
34. Liu, H.; Wang, P.; Schlesinger, R. A Numerical Study of Cirrus Clouds. Part II: Effects of Ambient Temperature, Stability, Radiation, Ice Microphysics, and Microdynamics on Cirrus Evolution. *J. Atmos. Sci.* **2003**, *60*, 1097–1119. [CrossRef]

35. Spichtinger, P.; Gierens, K. Modelling of cirrus clouds—Part 2: Competition of different nucleation mechanisms. *Atmos. Chem. Phys.* **2009**, *9*, 2319–2334. [CrossRef]
36. Unterstrasser, S.; Gierens, K. Numerical simulations of contrail-to-cirrus transition—Part 2: Impact of initial ice crystal number, radiation, stratification, secondary nucleation and layer depth. *Atmos. Chem. Phys.* **2010**, *10*, 2037–2051. [CrossRef]
37. Lewellen, D.C. Persistent contrails and contrail cirrus. Part 2: Full Lifetime Behavior. *J. Atmos. Sci.* **2014**, *71*, 4420–4438. [CrossRef]
38. Unterstrasser, S.; Sölch, I. Optimisation of simulation particle number in a Lagrangian ice microphysical model. *Geosci. Model Dev.* **2014**, *7*, 695–709. [CrossRef]
39. Paoli, R.; Shariff, K. Contrail Modeling and Simulation. *Annu. Rev. Fluid Mech.* **2016**, *48*, 393–427. [CrossRef]
40. Kaufmann, S.; Voigt, C.; Jeßberger, P.; Jurkat, T.; Schlager, H.; Schwarzenboeck, A.; Klingebiel, M.; Thornberry, T. In situ measurements of ice saturation in young contrails. *Geophys. Res. Lett.* **2014**, *41*, 702–709. [CrossRef]
41. Grewe, V.; Dahlmann, K. How ambiguous are climate metrics? Furthermore, are we prepared to assess and compare the climate impact of new air traffic technologies? *Atmos. Environ.* **2015**, *106*, 373–374. [CrossRef]
42. Bickel, M.; Ponater, M.; Bock, L.; Burkhardt, U.; Reineke, S. Estimating the Effective Radiative Forcing of Contrail Cirrus. *J. Clim.* **2020**, *33*, 1991–2005. [CrossRef]
43. Schumann, U.; Graf, K.; Mannstein, H. Potential to reduce the climate impact of aviation by flight level changes. In Proceedings of the 3rd AIAA Atmospheric and Space Environments Conference, Honolulu, HI, USA, 27–30 June 2011; Volume 3376, pp. 1–22. [CrossRef]
44. Schumann, U.; Heymsfield, A.J. On the Life Cycle of Individual Contrails and Contrail Cirrus. *Meteorol. Monogr.* **2017**, *58*, 3.1–3.24. [CrossRef]
45. Schumann, U.; Mayer, B.; Graf, K.; Mannstein, H. A Parametric Radiative Forcing Model for Contrail Cirrus. *J. Appl. Meteor. Climatol.* **2012**, *51*, 1391–1406. [CrossRef]
46. Crow, S. Stability theory for a pair of trailing vortices. *AIAA J.* **1970**, *8*, 2172–2179. [CrossRef]
47. Bier, A.; Burkhardt, U.; Bock, L. Synoptic Control of Contrail Cirrus Life Cycles and Their Modification Due to Reduced Soot Number Emissions. *J. Geophys. Res.* **2017**, *122*, 11584–11603, [CrossRef]
48. Paoli, R.; Thouron, O.; Cariolle, D.; García, M.; Escobar, J. Three-dimensional large-eddy simulations of the early phase of contrail-to-cirrus transition: effects of atmospheric turbulence and radiative transfer. *Meteorol. Z.* **2017**, *26*, 597–620. [CrossRef]
49. Grewe, V.; Stenke, A. AirClim: An efficient tool for climate evaluation of aircraft technology. *Atmos. Chem. Phys.* **2008**, *8*, 4621–4639. [CrossRef]
50. Marks, T.; Dahlmann, K.; Grewe, V.; Gollnick, V.; Linke, F.; Matthes, S.; Stumpf, E.; Unterstrasser, S.; Yamashita, H.; Zumegen, C. Climate Impact Mitigation Potential of Formation Flight. *Aerospace* **2020**, in review.
51. Dahlmann, K.; Matthes, S.; Yamashita, H.; Unterstrasser, S.and Grewe, V.; Marks, T. Assessing the climate impact of formation flights. *Aerospace* **2020**, in review.